Deep Ductile Shear Zone Facilitates Near-Orthogonal Strike-Slip Faulting in a Thin Brittle Lithosphere

Chao Liang, Jean Paul Ampuero, Daniel Pino Muñoz

AGU ADVANCING EARTH AND SPACE SCIENCE

Geophysical Research Letters

RESEARCH LETTER
10.1029/2020GL090744

Key Points:

- Simulations reveal shear bands in deep ductile layer induces orthogonal strike-slip faulting in thin brittle lithosphere
- Faults nucleated in brittle lithosphere are unlikely to form at orthogonal angles
- Low confining pressure at shallow depth facilitates near-orthogonal strike-slip faulting

Supporting Information:

- Supporting Information S1

Correspondence to:
C. Liang,
chao.liang@geoazur.unice.fr

Citation:
Liang, C., Ampuero, J.P., & Pino Muñoz, D. (2021). Deep ductile shear zone facilitates near-orthogonal strike-slip faulting in a thin brittle lithosphere. *Geophysical Research Letters*, *48*, e2020GL090744https://doi.org/10.1029/2020GL090744

Received 12 SEP 2020
Accepted 14 DEC 2020

Deep Ductile Shear Zone Facilitates Near-Orthogonal Strike-Slip Faulting in a Thin Brittle Lithosphere

Chao Liang[1], Jean-Paul Ampuero[1], and Daniel Pino Muñoz[2]

[1]Géoazur, Université Côte d'Azur, IRD, CNRS, Observatoire de la Côte d'Azur, Valbonne, France, [2]MINES ParisTech, PSL Research University, Centre de Mise en Forme des Matériaux, CNRS UMR 7635, Sophia Antipolis, France

Abstract Some active fault systems comprise near-orthogonal conjugate strike-slip faults, as highlighted by the 2019 Ridgecrest and the 2012 Indian Ocean earthquake sequences. In conventional Mohr-Coulomb failure theory, orthogonal faulting requires a zero frictional coefficient (pressure-insensitive), which is unlikely in the brittle lithosphere. The simulations developed here show that near-orthogonal faults can form in the brittle layer by inheriting the geometry of orthogonal shear zones nucleated in the deep ductile (pressure-insensitive) layer. In particular, if the brittle layer is sufficiently thinner than the ductile fault root, near-orthogonal faulting is preserved at the surface. The preservation is further facilitated by a depth-dependent strength in the brittle layer. Conversely, faults nucleated within the brittle layer are unlikely to form at orthogonal angles. Our model thus offers a possible explanation for orthogonal strike-slip faulting and reveals the significant interactions between the structure of faults in the brittle upper lithosphere and their deep ductile roots.

Plain Language Summary Some notable earthquakes have occurred on sets of horizontally sliding vertical faults that cross each other at almost right angles (90°). This is puzzling because the conventional theory of how Earth's brittle outer shell, the crust, breaks predicts a narrower angle between faults, close to 60°. Our work offers an explanation to this puzzle. Theory also predicts that faults can form at right angles in rocks whose strength does not depend on the pressure acting on them. This is precisely the case in the deep viscous rocks that lie below the crust. Our computer simulations show that a pair of faults formed at right angle in deep viscous rocks can then grow upwards, gradually evolving to the narrower angle expected in the crust. If the crust is too thin, the faults reach the surface with almost right angles. Our proposed mechanism is effective on brittle crusts that are thinner than their viscous roots, which is the case in some regions where faulting at right angle is observed. Thus, our results show that the ductile root has important effects on the geometry of faults in the crust.

1. Introduction

Several earthquake sequences have involved ruptures on conjugate orthogonal strike-slip faults (Figure 1): the 2012 Indian Ocean earthquake (Meng et al., 2012), the 2019 Ridgecrest sequence (Ross et al., 2019), the 1987 Superstitious Hills sequence (Hanks & Allen, 1989; Hudnut et al., 1989) and numerous others in Japan (Fukuyama, 2015; Thatcher & Hill, 1991). Orthogonal strike-slip faulting is puzzling because it contradicts the conventional Coulomb faulting theory, which predicts that, for typical values of rock friction coefficient of 0.6–0.9 (Byerlee, 1978; Jaeger et al., 2009), crustal conjugate faults should intersect at an angle of 48–60° (at 24–30° from the maximum principal stress σ_1). In that framework, a nearly orthogonal fault geometry implies a pressure-insensitive strength (a friction coefficient of zero or a ductile material), which is unlikely in the brittle lithosphere.

One proposed explanation is that orthogonal faults originally formed at a narrower angle consistent with Coulomb theory and then rotated with the host rock toward the current geometry (e.g., Freund, 1974; Nur et al., 1986). However, this theory relies on an ad hoc termination of rotation for faults to end up at nearly orthogonal angle (Thatcher & Hill, 1991) and substantial rock deformation at regional scale. It is also possible that the two crossing faults formed at different geological times or inherited structures from nonshear zone structures such as orthogonal opening mode fractures (e.g., joints and dikes) (e.g., d'Alessio & Martel, 2005; Martel, 1990; Segall & Pollard, 1980). Another possibility is a strong poroelastic effect inside the fault zone bringing the effective fault friction coefficient close to zero (Cocco & Rice, 2002). However, this

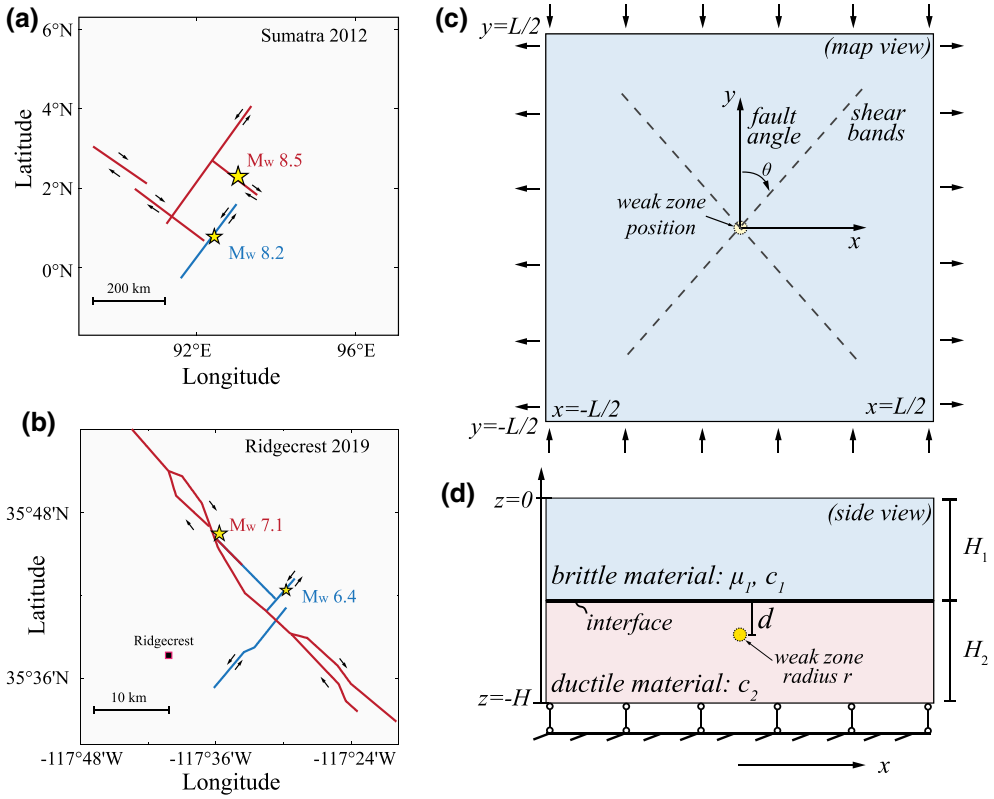

Figure 1. Schematics of orthogonal fault segments ruptured by 2012 Sumatra earthquake (a) and 2019 Ridgecrest sequence (b) (modified from Meng et al. (2012) and Ross et al. (2019)). The red traces mark the ruptured segments for the main shock (Mw 8.5 for Sumatra, Mw 7.1 for Ridgecrest) and the blue trace marks one notable aftershock (Mw 8.2, Sumatra) or foreshock (Mw 6.4, Ridgecrest). The black arrows indicate the direction of slip. (c)–(d) Map view and side view of 3D model geometry and boundary conditions (symbols are explained in the Model setup section).

hypothesis is in contradiction to the large stress drop observed during the rupture of orthogonal faults (Hill et al., 2015; Meng et al., 2012; Wei et al., 2013).

An alternative hypothesis, first proposed by Thatcher and Hill (1991), is that orthogonal strike-slip faults inherit their geometry from deep ductile shear zones. This hypothesis is supported by laboratory rock experiments in which shear bands appear at ~45° to σ_1 under lower crust pressure and temperature conditions (e.g., Shelton et al., 1981). In addition, geological observations of high-strain mylonite shear zones in the lower crust and upper mantle indicates the possibility of localization at high pressure and temperature conditions (Bürgmann & Dresen, 2008; Montési, 2013; White et al., 1980). Possible weakening mechanisms in the ductile roots include thermo-mechanical coupling induced by shear heating (e.g., Brun & Cobbold, 1980; Hobbs et al., 1986), grain size reduction (e.g., Montési & Hirth, 2003; Mulyukova & Bercovici, 2019), and phase transformations (e.g., Kirby, 1987; Green et al., 1990; Green Ii & Burnley, 1989).

However, it is unclear to what extent can the brittle layer preserve the orthogonal structure of deep contemporaneously nucleated ductile shear bands and what are the key controlling factors of such inheritance. In this work, we aim to address these questions by performing three-dimensional (3D) finite element simulations of faults modeled as plastic shear bands in a two-layered elastoplastic model. This minimalistic model captures the primary ingredients (contrast in pressure dependency between brittle and ductile layers) sufficient for testing our hypothesis while allowing us to distill fundamental understandings of the process.

2. Model Setup

Our simple 3D model features two layers ($k = 1$ upper, $k = 2$ lower) with a lateral length L, thickness H_k, Young's modulus E_k and Poisson's ratio ν_k, frictional coefficient μ_k, and cohesion c_k, as shown in Figures 1c and 1d. We solve the quasi-static balance of forces in elastoplastic solids with Drucker-Prager yielding criterion (e.g., Chemenda et al., 2016; Drucker & Prager, 1952; Duretz et al., 2018; Stefanov & Bakeev, 2014; Templeton & Rice, 2008) on a 3D unstructured grid using the parallel finite element code CIMLIB (Digonnet et al., 2007; Mesri et al., 2009). The yielding strength for Drucker-Prager rheology is: $S_k = \mu_k P + c_k$, where P is the effective pressure. Note that tension is positive in our convention. The two layers are coupled through the continuity of displacement and traction on the interface.

To avoid mesh-dependent results due to strain localization down to infinitesimal length scales, we incorporate dilatancy with a dilatancy coefficient β_1 such that $\beta_1 > 0.24\mu_1$ in the brittle layer (Templeton & Rice, 2008). In particular, we use $\mu_1 = 0.87$, $\beta_1 = 0.3$, and $c_1 = 10$ MPa, which gives a preferred faulting angle of $\theta \approx 30.4°$, the angle of the fault plane relative to the maximum compressive stress σ_1, well predicted by classic bifurcation theory (Chemenda, 2007; Rice, 1973; Rudnicki & Rice, 1975). We conducted one simulation with spontaneous strain localization in the brittle layer by setting $\mu_1 = 0.85$ and $\beta_1 = 0.1$, regularized by a nonlocal gradient-enhanced method (e.g., Jirásek & Grassl, 2004; R. Peerlings et al., 1995; R. H. Peerlings et al., 1998) described in supporting S1. However, a thorough study of the effect of strain localization is beyond the scope of this paper.

By setting $\mu_2 = 0$, we use the von Mises yield criterion in the deeper layer, which captures the pressure-insensitive nature of ductile materials (e.g., Besson, 2010; Mises, 1913; Schajer, 1994). In addition, we assume perfect plasticity, thus no hardening or weakening for c_2. As a result, strain localization is suppressed in the ductile layer and the shear zones are marked by bands with elevated but diffused plastic strain. By adopting a perfect von Mises plastic rheology instead of a more realistic, ductile rheology, we neglect the rate-dependent strength and bypass complex localization mechanisms, which enables us to focus on the effect of the contrast in pressure dependency between brittle and ductile layer. Due to the absence of pressure-dependency, the favored fault angle in the ductile layer is $\theta = 45°$.

We nucleate the shear band by prescribing a spherical weak zone with radius r, zero friction, zero dilatancy, and a weakened cohesion $c_w = 0.1c_1$ at the center of the domain in the map view ($x = 0$ and $y = 0$) but varying vertical position z_w. The distance from the centroid of the weak zone to the material interface is denoted as $d = z_w + H_1$. Note that $d > 0$ denotes weak zone in the upper layer and $d < 0$ in the lower layer. The weak zone concentrates stresses in its vicinity, which initiates two conjugate shear bands.

We set up a bi-axial loading boundary condition to mimic a strike-slip environment, as shown in Figures 1c and 1d. The bottom surface ($z = -H$) is constrained in vertical displacement. The deformation is driven by shortening in one horizontal direction (y) and extension in the other (x) by the same normal velocity magnitude V. Since the body force (gravity) does not change over time, it is incorporated as an initial stress.

We start with an initial condition of zero deviatoric stresses and experiment two types of initial pressure P_0: uniform and linearly increasing with depth (due to gravity). To be consistent with the initial pressure, the top surface ($z = 0$) is constrained in vertical displacement when P_0 is uniform and set as traction free when P_0 is depth-dependent. As we shall see in the next section, the case of uniform P_0, though simple, captures the major characteristics of fault angle. We run the simulation until time t so that the approximate loading strain $\epsilon = Vt/L$ is 50% above the yielding strain of the upper layer ($S_1/2G_1$), where G_1 is the shear modulus. Finally, the fault angle at each depth slice is extracted (see supplementary material).

3. Results

Our simulations produce two conjugate faults (Figures 2a and 2b of the same length. Due to the simplicity of our model, we do not produce different fault lengths or multiple fault segments as in the real examples shown in Figure 1. We focus on analyzing how the fault angle θ depends on depth, and what factors control this depth-dependence. We systematically identified the essential parameters based on dimensional analysis (Barenblatt, 1996) (see supporting S1) and exploratory simulations by varying one parameter at a time

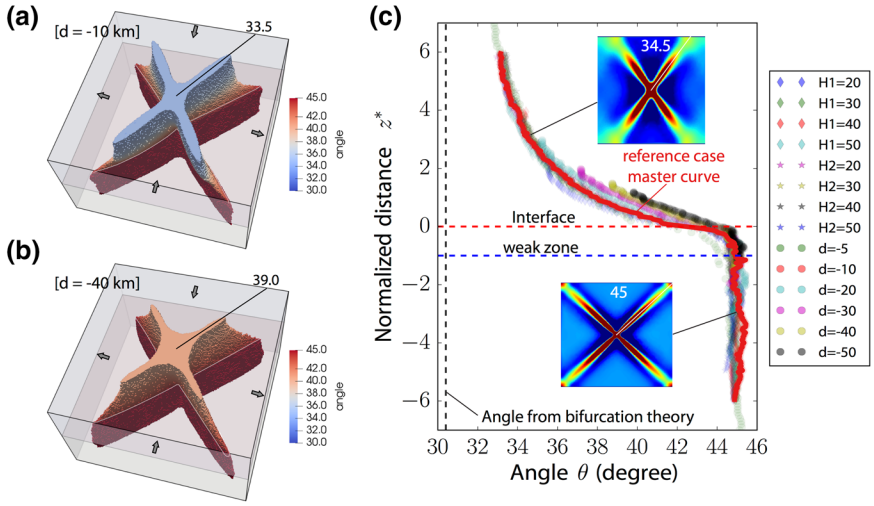

Figure 2. (a–b) Three-dimensional fault structure (represented by region with plastic strain higher than the 95% quantile values) in two simulations with different nucleation positions (−10 and −40 km) below the interface. Colors indicate the fault angle at each depth and arrows indicate the loading condition. (c) Fault angle θ as a function of normalized vertical position z^* (red master curve for reference case, dots for varying parameters). Parameters for the reference model are $L = 200$ km, $d = -10$ km, and $H_1 = H_2 = 60$ km. The vertical gray dashed line marks the faulting angle (30.4°) predicted by bifurcation theory for the brittle layer. To first order, all simulations collapse onto the same master curve after normalization. The two insets show the final plastic strain at two depths (color saturates at the 10% and 95% quantile values), highlighting the difference of faulting angles.

with respect to the reference cases: $H_1 = H_2 = 60$ km, $L = 200$ km, $d = \pm 10$ km, $E_{2r} = E_2/E_1 = 1.0$, $S_{2r} = S_2/S_1 = 1.0$. We first vary various lengths scales (H_1, H_2, d, and L) to determine the proper dimensionless position z^* that characterizes the depth variation of θ. We then explore the effect of a weaker ductile layer with $E_{2r} = E_2/E_1 < 1$ and $S_{2r} = S_2/S_1 < 1$. Finally, we present the effect of depth-varying shear strength on the fault angle. The sensitivity of fault angle to lateral model size L and the size of the weak zone r are examined in the supplementary material. Both effects are small when the model size is sufficiently large and the weak zone sufficiently small.

The most important factor controlling the persistence of orthogonal faulting up to the surface is the position d of the weak zone relative to the material interface. After representing the fault angle θ as a function of a normalized depth $z^* = (z + H_1)/|d|$, the results from simulations with different values of $|d|$, H_1, and H_2 collapse onto two master curves, corresponding to nucleation within the ductile (Figures 2c) and brittle layers (Figure 3c), respectively. The convergence to the red master curve is closer at depths away from the top and bottom boundaries.

Shear bands nucleated in the ductile layer form at an angle $\theta = 45°$ and progressively twist, as they propagate upwards, toward the preferred angle $\theta_b \sim 30.4°$ predicted by bifurcation theory in the brittle layer. This twist results in a helical fault shape. Changing μ_1 and β_1 changes the value of θ_b but does not alter the shape of the curve if θ is normalized as $\theta^* = (\theta - \theta_b)/(45 - \theta_b)$ (see supplementary material). Approximately, the fault angle solely depends on z^* and not on other length scales such as the size of the model or thickness of both layers, provided these boundaries are far from the interface and from the nucleation zone. A relatively thinner upper crust (i.e., as H_1 becomes much smaller than $|d|$) favors inheritance of the deep faulting angle at the surface (Figures 2b and 2c). For instance, given $H_1/|d| = 0.5$, the fault angle at the surface is ~42° and the two conjugate faults are nearly orthogonal. As $|d|$ increases (a weak zone closer to bottom boundary, dots in Figure 2c), the trend of fault angle deviates more from the master curve in the way that favors inheritance, probably due to a stronger boundary effect.

The contrast of shear strength and elastic stiffness have very limited influence on the general trend of shear band rotation, regardless of nucleation depth (Figure S5). Nevertheless, a weaker ductile layer does make orthogonal faulting in the upper crust more difficult: reducing both E_{2r} and S_{2r} to 0.1 reduces the fault angle

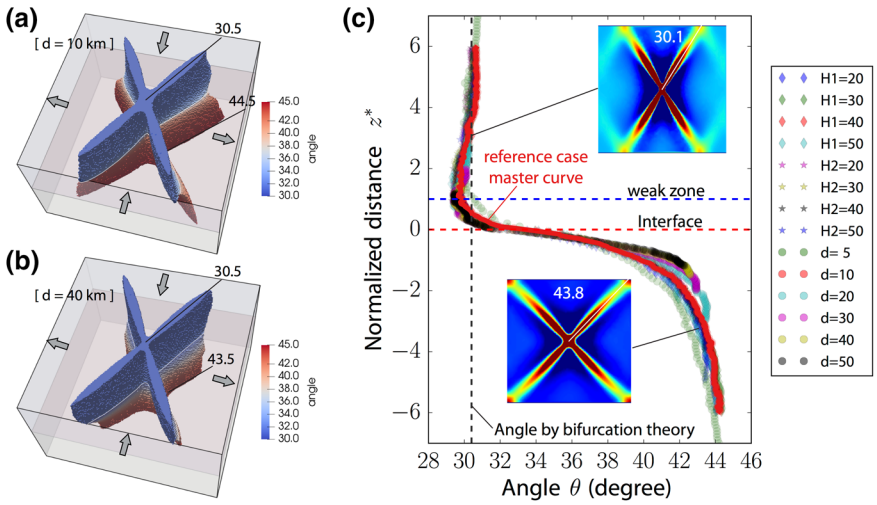

Figure 3. Same as Figure 2 but for nucleation in the brittle layer ($d > 0$) and a reference model with $d = 10$ km. The fault angle in the brittle layer is near-optimal and rotates toward 45° in the ductile layer.

by ~2°. Our current nucleation scheme is not effective in the ductile layer with a more extreme strength contrast because the strength contrast between the weak zone and the host rock diminishes as the host rock itself is extremely weak.

Near-orthogonal faults are very unlikely to be initiated in the brittle layer. Indeed, faults nucleated in the brittle layer tend to orient at the optimal angle ($\theta_b \sim 30.4°$) throughout the upper layer (Figure 3a). They rapidly rotate toward 45° inside the ductile layer. Yet, since the length scale for fault angle change as a function of depth is $|d|$, bands formed by a shallower nucleation (a larger d) can cut deeper into the ductile layer, dragging the deep fault angle substantially away from 45°.

Mechanism of inheritance of orthogonal faulting remains viable under depth-dependent shear strength. We conducted simulations using a linear increase of shear strength in the top 20 km (due to lithostatic initial pressure) followed by an exponential decay due to the rising temperature (Figure 4a). We bound the strength profile at depth at a minimum of 10 MPa because otherwise our artificial nucleation in the ductile layer would be inefficient, due to the small contrast in strength between the weak zone and the host rock and the absence of weakening in our perfect plasticity model. As shown in Figure 4b, the depth-dependent shear strength does not alter the general characteristics of fault angle rotation revealed by our previous minimalistic model with uniform strength (Figures 2 and 3). For faults nucleated in the ductile layer, the fault angle approximately follows the master curve of the simpler model close to the material interface. Approximately above the middle of the upper layer, deviation occurs and the fault angle stops approaching closer to 30°, which favors inheriting deep structures. Since a weaker ductile layer has limited impact on the fault angle when the initial pressure is uniform (Figure S5), this deviation is likely due to a lower confining pressure at shallower depth. Shallow near-orthogonal faulting ($\theta > 42°$) occurs if $H_1/|d| < \sim 1$, a broader range than in the simple model. Faults nucleated in the brittle layer as shown in Figure 4b exhibit a more complex pattern of rotation. Their fault angle approximately follows the master curve of the uniform-strength model only for z^* in the range $\sim[-2, 0]$. In particular, the lower strength at shallow depth introduces a reversal in the trend of fault angle near the free surface.

4. Discussion

Our results reveal the important control of thickness of the brittle layer (H_1) and the position of the weak zone (d) on the orientation of the fault angle. Although $|d|$ is generally unknown in real faults, it is bounded by the largest depth below the brittle lithosphere at which spontaneous ductile shear localization can occur. This in turn is bounded by the thickness of the ductile lithosphere H_2, which we take here as the reference

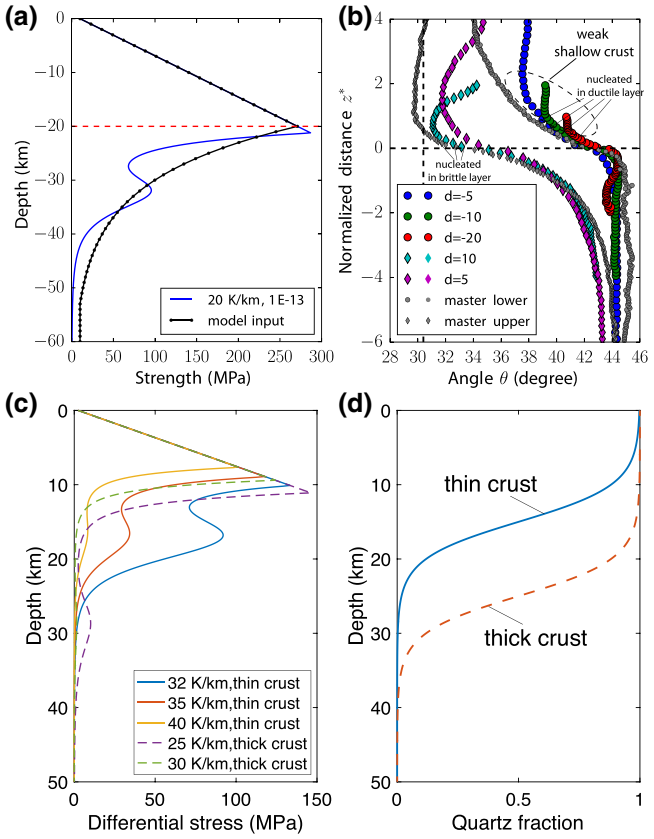

Figure 4. (a) Fault angle θ as a function of normalized distance z^* with a depth-dependent shear strength for different nucleation positions d (see legend, in km). Master curves (gray symbols) are the results with $d = \pm 10$ km from models with uniform shear strength. The gray vertical dashed line marks the preferred angle for the upper layer from bifurcation theory. (b) Shear strength as a function of depth assumed in our model (black) and, for comparison, based on the rheological parameters in Allison and Dunham (2018) with a thermal gradient of 20 K/km and strain rate of 10^{-13} s^{-1}. (c) Shear strength profile with different geothermal gradients and compositions for a thick and thin crust. (d) Fraction of quartz, (see text for more explanation of the rheology model used). Note the thicker ductile root for a thin crust due to an upward shift of more mafic composition.

length scale. According to our model, for near-orthogonal faults (say, $\theta > 42°$) to be observed near the surface, the nucleation must occur in the ductile layer and $H_1/|d| < 1$. The latter condition is always satisfied if $H_1/H_2 < 1$. Thus, this mechanism works best for a thin brittle layer and a thick ductile root.

We now connect the model results to natural faults. The depth distribution of crustal earthquakes delineates the extent of a seismogenic zone, which is usually associated with the depth of the brittle-ductile transition (BDT) (Bürgmann & Dresen, 2008; Burov, 2011; Hauksson & Meier, 2019; Kohlstedt et al., 1995; Scholz, 1988; Zuza & Cao, 2020) or the transition of frictional behavior from velocity-weakening to velocity-strengthening within the brittle layer (Tse & Rice, 1986). Furthermore, the BDT is rather a zone of semi-brittle to ductile behavior (Kohlstedt et al., 1995), which can be particularly broad for oceanic lithosphere with moderate to old age and high strength. Despite these caveats and others noted by, for example, Déverchère et al. (2001), we place the BDT at the reported seismogenic depth and also use its depth as a proxy for the thickness of the brittle layer. The ductile layer is defined as a zone below the BDT and with a strength higher than a few MPa (Kohlstedt et al., 1995; Ranalli, 1997). With these assumptions in mind, we next confront our model predictions with available observations.

In continental plates, orthogonal strike-slip faulting appears to be particularly developed in relatively extensional environments marked by elevated heat flow and recent volcanism (Thatcher & Hill, 1991). In light of our model, we further posit that these regions are likely to have a thin brittle layer overlaying a comparatively thick ductile root. A thin seismogenic upper crust and high heat flow is indeed observed both near Ridgecrest (10.5–11 km) and Salton Trough (~10 km) (Hauksson & Meier, 2019; Ross et al., 2019; Zuza & Cao, 2020). In addition, active rifting in Salton Trough (Lekic et al., 2011; Barak et al., 2015) and vigorous Quaternary volcanism in the Coso region (Bacon et al., 1981) may have contributed to magma underplating, that is, the intrusion of mafic partial melt into the lower crust (Thybo & Artemieva, 2013). As a result, the lower crust can be significantly more mafic than the upper crust and remain strong up to higher temperatures (Albaric et al., 2009; Hirth & Kohlstedf, 2003; Kohlstedt et al., 1995). We illustrate the effect of underplating with a simple two-phase rheology model that smoothly mixes quartz (upper crust) and olivine (upper mantle) using the mixing law from Ji et al. (2003) (more details in supporting information): a shallower transition to more mafic composition produces a long ductile tail in a thin crust at high geothermal gradients of 35–40 K/km (Figures 4c and 4d). In this case, the brittle and ductile layers have comparable thickness and our model with shear bands nucleated in the ductile layer predicts near-orthogonal faulting up to the surface. Shallow Moho depths, observed near Ridgecrest (26–28 km) and Salton Trough (18–22 km) (Parsons & McCarthy, 1996; Yan & Clayton, 2007; Zhu & Kanamori, 2000), seem to support this interpretation.

The oceanic lithosphere contains a very thin crust and a cooled upper mantle characterized by a broad brittle-plastic transition and high strength as the plate ages (Burov, 2011; Jain et al., 2017; Kohlstedt et al., 1995). In Wharton basin, the great 2012 Indian Ocean earthquake ruptured the entire oceanic crust and penetrated as deep as 50–60 km into the lithospheric mantle through a set of near-orthogonal fault segments (Hill et al., 2015; Kwong et al., 2019; Meng et al., 2012; Singh et al., 2017; Wei et al., 2013). The BDT depth defined by the 600°C isotherm for this 45–65 Ma old lithosphere is around 30–35 km (Hill et al., 2015; Kwong et al., 2019). The initiation of frictional failure is generally considered unlikely at higher temperature (Abercrombie & Ekström, 2001; Hill et al., 2015; McGuire & Beroza, 2012). If we regard the upper 30 km as

brittle with the ductile layer extending at least to a depth of 50–60 km where seismicity terminates, the ratio H_1/H_2 would be close to 1. Thus, we consider the Wharton basin another place where our model may be applicable.

In this first attempt to quantify fault angle in 3D, we kept the model as simple as possible and left out important mechanisms such as strain weakening and damage in the brittle material (Chemenda et al., 2016; Finzi et al., 2009; Herrendörfer et al., 2018; Stefanov & Bakeev, 2014), viscous flow (Duretz et al., 2018; Meyer et al., 2017), and weakening in the ductile layer for instance by grain size reduction (e.g., Montési & Hirth, 2003; Mulyukova & Bercovici, 2019). We also chose dilatancy values high enough to suppress strain localization, which in turn prevents mesh dependency in our simulations. The absence of weakening and thus the lack of effective strain localization results in a pair of smooth and broad shear bands with strains only slightly higher than the surrounding region and the plastic failure is distributed. We also explored the effect of spontaneous strain localization in the brittle layer (see supporting S1 and Figure S10). We find that the inheritance of ductile shear structure is still viable in the brittle layer, despite additional complexity (see supporting S1 and Figures S11 and S12). However, a thorough parametric study of models accounting for strain-softening behavior of brittle material and localization mechanisms in a rate-dependent ductile material remains to be addressed by a follow-up study. Dynamic rupture effects are also neglected in this study and could play an important role. In particular, Preuss et al. (2019) show that the fault angle grows differently during quasi-static nucleation and dynamic rupture.

5. Conclusion

Nearly orthogonal strike-slip faults in the brittle lithosphere can originate from deep ductile shear zone, provided the brittle layer is not thicker than the depth extent of the ductile roots of the faults. Low confining pressure at shallow depth further facilitates the formation of the near-orthogonal structure. Geophysical observations in the Wharton basin seem compatible with this interpretation. In the Salton Trough and Ridgecrest areas, a shallow Moho and tectonic activities (active rifting and Quaternary volcanism) possibly facilitate a stronger underplating in the lower crust, which could give rise to a thin upper crust and relatively thicker ductile root at high heat flow, favorable for orthogonal faulting. Conversely, fault nucleation in the brittle layer tends to generate conjugate fault angles close to the optimal value predicted by bifurcation theory and is thus insufficient to generate nearly orthogonal faults. Future work shall extend the current model by incorporating weakening mechanisms that lead to strain localization in both brittle and ductile layers. Such models can then provide consistent fault geometries and initial stresses for dynamic rupture modeling to study the mechanics of earthquakes on orthogonal faults. Overall, our modeling results advance the mechanical understanding of the geometry of strike-slip faults from the Earth's surface to their ductile roots.

Data Availability Statement

Except for Figure 1 (modified from Meng et al. (2012) and Ross et al. (2019)), all other data are generated by numerical simulations. The python scripts used to generate CIMLIB input files are contained in the Zenodo data repository (Liang et al., 2020). Figures 2–4 are readily reproducible using the processed data and IPython scripts contained in the Zenodo data repository (Liang et al., 2020). 3D visualizations are performed using Paraview (Ayachit, 2015) and meshes are generated using Gmsh (Geuzaine & Remacle, 2009), both of which are open source and freely accessible. The finite element code CIMLIB developed at Mines ParisTech is not open source but is available through a fairly standard procedure upon contacting the CEMEF center.

Acknowledgments
This work was supported by the French government through the UCAJEDI Investments in the Future project (grant ANR-15-IDEX-01) managed by the National Research Agency (ANR). We thank Huihui Weng and Martijn van den Ende for inspiring discussions. Simulations were performed on the CEMEF cluster at Mines ParisTech.

References

Abercrombie, R. E., & Ekström, G. (2001). Earthquake slip on oceanic transform faults. *Nature*, *410*(6824), 74–77.
Albaric, J., Déverchère, J., Petit, C., Perrot, J., & Le Gall, B. (2009). Crustal rheology and depth distribution of earthquakes: Insights from the central and southern east African rift system. *Tectonophysics*, *468*(1–4), 28–41.
Allison, K. L., & Dunham, E. M. (2018). Earthquake cycle simulations with rate-and-state friction and power-law viscoelasticity. *Tectonophysics*, *733*, 232–256.
Ayachit, U. (2015). *The paraview guide: A parallel visualization application*. Kitware, Inc.

Bacon, C. R., Macdonald, R., Smith, R. L., & Baedecker, P. A. (1981). Pleistocene high-silica rhyolites of the Coso Volcanic Field, Inyo County, California. *Journal of Geophysical Research*, *86*(B11), 10223–10241. https://doi.org/10.1029/JB086iB11p10223
Barak, S., Klemperer, S. L., & Lawrence, J. F. (2015). San Andreas Fault dip, Peninsular Ranges mafic lower crust and partial melt in the Salton Trough, Southern California, from ambient-noise tomography. *Geochemistry, Geophysics, Geosystems*, *16*(11), 3946–3972.
Barenblatt, G.I. (1996). Scaling, self-similarity, and intermediate asymptotics: Dimensional analysis and intermediate asymptotics. (14). Cambridge University Press.
Besson, J. (2010). Continuum models of ductile fracture: A review. *International Journal of Damage Mechanics*, *19*(1), 3–52.
Brun, J., & Cobbold, P. (1980). Strain heating and thermal softening in continental shear zones: A review. *Journal of Structural Geology*, *2*(1–2), 149–158.
Bürgmann, R., & Dresen, G. (2008). Rheology of the lower crust and upper mantle: Evidence from rock mechanics, geodesy, and field observations. *Annual Review of Earth and Planetary Sciences*, *36*, 531–567.
Burov, E. B. (2011). Rheology and strength of the lithosphere. *Marine and Petroleum Geology*, *28*(8), 1402–1443.
Byerlee, J. (1978). Friction of rocks. In *Rock friction and earthquake prediction* (pp. 615–626). Springer.
Chemenda, A. I. (2007). The formation of shear-band/fracture networks from a constitutive instability: Theory and numerical experiment. *Journal of Geophysical Research*, *112*(B11). https://doi.org/10.1029/2007JB005026
Chemenda, A. I., Cavalie, O., Vergnolle, M., Bouissou, S., & Delouis, B. (2016). Numerical model of formation of a 3-D strike-slip fault system. *Comptes Rendus Geoscience*, *348*(1), 61–69.
Cocco, M., & Rice, J. R. (2002). Pore pressure and poroelasticity effects in Coulomb stress analysis of earthquake interactions. *Journal of Geophysical Research*, *107*(B2), ESE 2-1–ESE 2-17. https://doi.org/10.1029/2000JB000138
Déverchère, J., Petit, C., Gileva, N., Radziminovitch, N., Melnikova, V., & San'Kov, V. (2001). Depth distribution of earthquakes in the Baikal rift system and its implications for the rheology of the lithosphere. *Geophysical Journal International*, *146*(3), 714–730.
Digonnet, H., Silva, L., & Coupez, T. (2007). Cimlib: A fully parallel application for numerical simulations based on components assembly. *AIP Conference Proceedings*, *908*, 269–274.
Drucker, D. C., & Prager, W. (1952). Soil mechanics and plastic analysis or limit design. *Quarterly of Applied Mathematics*, *10*(2), 157–165.
Duretz, T., Souche, A., De Borst, R., & Le Pourhiet, L. (2018). The benefits of using a consistent tangent operator for viscoelastoplastic computations in geodynamics. *Geochemistry, Geophysics, Geosystems*, *19*, 4904–4924. https://doi.org/10.1029/2018GC007877
d'Alessio, M., & Martel, S. J. (2005). Development of strike-slip faults from dikes, Sequoia National Park, California. *Journal of Structural Geology*, *27*(1), 35–49.
Finzi, Y., Hearn, E. H., Ben-Zion, Y., & Lyakhovsky, V. (2009). Structural properties and deformation patterns of evolving strike-slip faults: Numerical simulations incorporating damage rheology. *Pure and Applied Geophysics*, *166*(10–11), 1537–1573.
Freund, R. (1974). Kinematics of transform and transcurrent faults. *Tectonophysics*, *21*(1–2), 93–134. 10.1016/0040-1951(74)90064-X
Fukuyama, E. (2015). Dynamic faulting on a conjugate fault system detected by near-fault tilt measurements. *Earth Planets and Space*, *67*(1), 38.
Geuzaine, C., & Remacle, J.-F. (2009). Gmsh: A 3-d finite element mesh generator with built-in pre-and post-processing facilities. *International Journal for Numerical Methods in Engineering*, *79*(11), 1309–1331.
Green Ii, H., & Burnley, P. (1989). A new self-organizing mechanism for deep-focus earthquakes. *Nature*, *341*(6244), 733.
Green, H. W., Young, T. E., Walker, D., & Scholz, C. H. (1990). Anticrack-associated faulting at very high pressure in natural olivine. *Nature*, *348*(6303), 720–722.
Hanks, T. C., & Allen, C. R. (1989). The Elmore Ranch and Superstition Hills earthquakes of 24 November 1987: Introduction to the special issue. *Bulletin of the Seismological Society of America*, *79*(2), 231–238.
Hauksson, E., & Meier, M.-A. (2019). Applying depth distribution of seismicity to determine thermo-mechanical properties of the seismogenic crust in southern California: Comparing lithotectonic blocks. *Pure and Applied Geophysics*, *176*(3), 1061–1081.
Herrendörfer, R., Gerya, T., & Van Dinther, Y. (2018). An invariant rate-and state-dependent friction formulation for viscoeastoplastic earthquake cycle simulations. *Journal of Geophysical Research: Solid Earth*, *123*, 5018–5051. https://doi.org/10.1029/2017JB015225
Hill, E. M., Yue, H., Barbot, S., Lay, T., Tapponnier, P., Hermawan, I., et al. (2015). The 2012 mw 8.6 Wharton Basin sequence: A cascade of great earthquakes generated by near-orthogonal, young, oceanic mantle faults. *Journal of Geophysical Research: Solid Earth*, *120*, 3723–3747. https://doi.org/10.1002/2014JB011703
Hirth, G., & Kohlstedf, D. (2003). Rheology of the upper mantle and the mantle wedge: A view from the experimentalists. *Geophysical Monograph-American Geophysical Union*, *138*, 83–106.
Hobbs, B., Ord, A., & Teyssier, C. (1986). Earthquakes in the ductile regime? *Pure and Applied Geophysics*, *124*(1–2), 309–336.
Hudnut, K. W., Seeber, L., & Pacheco, J. (1989). Cross-fault triggering in the November 1987 Superstition Hills earthquake sequence, southern California. *Geophysical Research Letters*, *16*(2), 199–202.
Jaeger, J. C., Cook, N. G., & Zimmerman, R. (2009). *Fundamentals of rock mechanics*. John Wiley & Sons.
Jain, C., Korenaga, J., & Karato, S.-i. (2017). On the yield strength of oceanic lithosphere. *Geophysical Research Letters*, *44*(19), 9716–9722.
Jirásek, M., & Grassl, P. (2004). *Nonlocal plastic models for cohesive-frictional materials. Modelling of cohesive-frictional materials*. Proceedings of 2nd international symposium on continuous and discontinuous modelling of cohesive-frictional materials (cdm 2004), held in Stuttgart 27–28 sept. 2004 (pp. 323).
Ji, S., Zhao, P., & Xia, B. (2003). Flow laws of multiphase materials and rocks from end-member flow laws. *Tectonophysics*, *370*(1–4), 129–145.
Kirby, S. H. (1987). Localized polymorphic phase transformations in high-pressure faults and applications to the physical mechanism of deep earthquakes. *Journal of Geophysical Research*, *92*(B13), 13789–13800.
Kohlstedt, D., Evans, B., & Mackwell, S. (1995). Strength of the lithosphere: Constraints imposed by laboratory experiments. *Journal of Geophysical Research*, *100*(B9), 17587–17602.
Kwong, K. B., DeShon, H. R., Saul, J., & Thurber, C. H. (2019). Constraining the oceanic lithosphere seismogenic zone using teleseismic relocations of the 2012 Wharton Basin great earthquake sequence. *Journal of Geophysical Research: Solid Earth*, *124*, 11938–11950. https://doi.org/10.1029/2019JB017549
Lekic, V., French, S. W., & Fischer, K. M. (2011). Lithospheric thinning beneath rifted regions of southern California. *Science*, *334*(6057), 783–787.
Liang, C., Ampuero, J.-P., & Pino Muñoz, D. (2020). *Dataset for "Deep ductile shear localization facilitates near-orthogonal strike-slip faulting in a thin brittle lithosphere"*. Zenodo. https://doi.org/10.5281/zenodo.3940460
Martel, S. (1990). Formation of compound strike-slip fault zones, Mount Abbot quadrangle, California. *Journal of Structural Geology*, *12*(7), 869–882.

McGuire, J. J., & Beroza, G. C. (2012). A rogue earthquake off Sumatra. *Science*, *336*(6085), 1118–1119.
Meng, L., Ampuero, J.-P., Stock, J., Duputel, Z., Luo, Y., & Tsai, V. (2012). Earthquake in a maze: Compressional rupture branching during the 2012 Mw 8.6 Sumatra earthquake. *Science*, *337*(6095), 724–726.
Mesri, Y., Digonnet, H., & Coupez, T. (2009). Advanced parallel computing in material forming with cimlib. *European Journal of Computational Mechanics/Revue Européenne de Mécanique Numérique*, *18*(7–8), 669–694.
Meyer, S. E., Kaus, B. J., & Passchier, C. (2017). Development of branching brittle and ductile shear zones: A numerical study. *Geochemistry, Geophysics, Geosystems*, *18*(6), 2054–2075.
Mises, R. v. (1913). Mechanik der festen körper im plastisch-deformablen zustand. Nachrichten von der Gesellschaft der Wissenschaften zu Göttingen. *Mathematisch-Physikalische Klasse*, *1913*, 582–592.
Montési, L. G. (2013). Fabric development as the key for forming ductile shear zones and enabling plate tectonics. *Journal of Structural Geology*, *50*, 254–266.
Montési, L. G., & Hirth, G. (2003). Grain size evolution and the rheology of ductile shear zones: From laboratory experiments to postseismic creep. *Earth and Planetary Science Letters*, *211*(1–2), 97–110.
Mulyukova, E., & Bercovici, D. (2019). The generation of plate tectonics from grains to global scales: A brief review. *Tectonics*, *38*(12), 4058–4076.
Nur, A., Ron, H., & Scotti, O. (1986). Fault mechanics and the kinematics of block rotations. *Geology*, *14*(9), 746–749. 10.1130/0091-7613(1986)14⟨746:FMATKO⟩2.0.CO;2
Parsons, T., & McCarthy, J. (1996). Crustal and upper mantle velocity structure of the Salton Trough, southeast California. *Tectonics*, *15*(2), 456–471.
Peerlings, R., De Borst, R., Brekelmans, W., & De Vree, J. (1995). *Computational plasticity, fundamentals and applications. Computational modelling of gradient-enhanced damage for fracture and fatigue problems* (pp. 975–986). Proceedings of the 4th international conference.
Peerlings, R. H., de Borst, R., Brekelmans, W., & Geers, M. G. (1998). Gradient-enhanced damage modelling of concrete fracture. *Mechanics of Cohesive-Frictional Materials*, *3*(4), 323–342.
Preuss, S., Herrendörfer, R., Gerya, T., Ampuero, J.-P., & van Dinther, Y. (2019). Seismic and aseismic fault growth lead to different fault orientations. *Journal of Geophysical Research: Solid Earth*, *124*, 8867–8889. https://doi.org/10.1029/2019JB017324
Ranalli, G. (1997). Rheology and deep tectonics. *Annals of Geophysics*, *40*(3), 671–680. https://doi.org/10.4401/ag-3893
Rice, J. R. (1973). The initiation and growth of shear bands. In A. C. Palmer (Ed.), *Plasticity and soil mechanics* (pp. 263–274). Cambridge: Cambridge University Engineering Department.
Ross, Z. E., Idini, B., Jia, Z., Stephenson, O. L., Zhong, M., Wang, X., et al. (2019). Hierarchical interlocked orthogonal faulting in the 2019 ridgecrest earthquake sequence. *Science*, *366*(6463), 346–351. https://doi.org/10.1126/science.aaz0109
Rudnicki, J. W., & Rice, J. (1975). Conditions for the localization of deformation in pressure-sensitive dilatant materials. *Journal of the Mechanics and Physics of Solids*, *23*(6), 371–394.
Schajer, G. (1994). A teaching note on failure criteria and failure surfaces for ductile and brittle materials. *International Journal of Mechanical Engineering Education*, *22*(1), 1–13.
Scholz, C. (1988). The brittle-plastic transition and the depth of seismic faulting. *Geologische Rundschau*, *77*(1), 319–328.
Segall, P., & Pollard, D. (1980). Mechanics of discontinuous faults. *Journal of Geophysical Research*, *85*(B8), 4337–4350.
Shelton, G. L., Tullis, J., & Tullis, T. (1981). Experimental high temperature and high pressure faults. *Geophysical Research Letters*, *8*(1), 55–58.
Singh, S. C., Hananto, N., Qin, Y., Leclerc, F., Avianto, P., & Tapponnier, P. E., et al. (2017). The discovery of a conjugate system of faults in the Wharton Basin intraplate deformation zone. *Science Advances*, *3*(1), e1601689.
Stefanov, Y. P., & Bakeev, R. (2014). Deformation and fracture structures in strike-slip faulting. *Engineering Fracture Mechanics*, *129*, 102–111.
Templeton, E. L., & Rice, J. R. (2008). Off-fault plasticity and earthquake rupture dynamics: 1. dry materials or neglect of fluid pressure changes. *Journal of Geophysical Research*, *113*(B9), B09306.
Thatcher, W., & Hill, D. P. (1991). Fault orientations in extensional and conjugate strike-slip environments and their implications. *Geology*, *19*(11), 1116–1120.
Thybo, H., & Artemieva, I. M. (2013). Moho and magmatic underplating in continental lithosphere. *Tectonophysics*, *609*, 605–619.
Tse, S. T., & Rice, J. R. (1986). Crustal earthquake instability in relation to the depth variation of frictional slip properties. *Journal of Geophysical Research*, *91*(B9), 9452–9472.
Wei, S., Helmberger, D., & Avouac, J.-P. (2013). Modeling the 2012 Wharton basin earthquakes off-Sumatra: Complete lithospheric failure. *Journal of Geophysical Research: Solid Earth*, *118*(7), 3592–3609.
White, S., Burrows, S., Carreras, J., Shaw, N., & Humphreys, F. (1980). On mylonites in ductile shear zones. *Journal of Structural Geology*, *2*(1–2), 175–187.
Yan, Z., & Clayton, R. (2007). Regional mapping of the crustal structure in southern California from receiver functions. *Journal of Geophysical Research*, *112*(B5).
Zhu, L., & Kanamori, H. (2000). Moho depth variation in southern California from teleseismic receiver functions. *Journal of Geophysical Research*, *105*(B2), 2969–2980.
Zuza, A. V., & Cao, W. (2020). Seismogenic thickness of California: Implications for thermal structure and seismic hazard. *Tectonophysics*, *782–783*, 228426.